ACS APPLIED MATERIALS & INTERFACES

www.acsami.org

Research Article

Intercalation of Polyacrylonitrile Nanoparticles in $Ti_3C_2T_x$ MXene Layers for Improved Supercapacitance

Shanna Marie M. Alonzo, Shrabani De, Vanessa Morris, Daniel E. Autrey, Bhoj Raj Gautam, Gayani Pathiraja, and Bishnu Prasad Bastakoti*

Cite This: *ACS Appl. Mater. Interfaces* 2024, 16, 64784−64796

Read Online

ACCESS | Metrics & More | Article Recommendations | Supporting Information

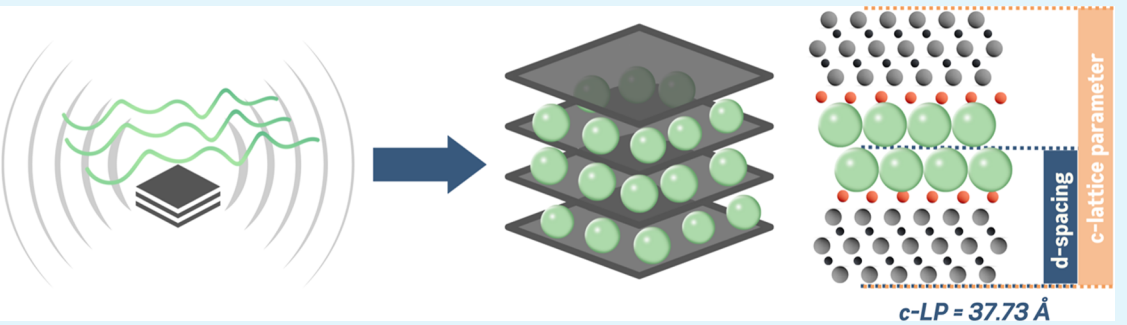

ABSTRACT: We report the intercalation of polyacrylonitrile nanoparticles in $Ti_3C_2T_x$ MXene layers through simple sonication. The use of polyacrylonitrile, which was synthesized via radical polymerization, offered dual benefits: (1) It increased the interlayer spacing of MXene, thereby exposing more surface area and enhancing ion transport channels during charge and discharge cycles, and (2) Integrating MXene with polyacrylonitrile enables the creation of a composite with conductive properties, following percolation principle. X-ray diffraction analysis showed an increase in the c-lattice parameter, indicative of the interlayer spacing, from 22.31 Å for the pristine MXene to 37.73 Å for the MXene−polyacrylonitrile composite. The intercalated polyacrylonitrile nanoparticles facilitated the delamination by weakening the interlayer interactions, especially during sonication. Electrochemical assessments revealed significant improvement in the properties of the MXene−polyacrylonitrile composite compared to the pristine MXene. The assembled asymmetric device achieved a good specific capacitance of 32.1 F/g, an energy density of 11.42 W h/kg, and 82.2% capacitance retention after 10,000 cycles, highlighting the practical potential of the MXene−polyacrylonitrile composite.

KEYWORDS: *MXenes, polymer, nanocomposites, supercapacitor, energy storage*

1. INTRODUCTION

MXenes are carbides/nitrides/carbonitrides of transition metals derived from MAX phase precursors, whose general formula is $M_{n+1}AX_n$ where M is a transition metal (Ti, V, Cr, Mn, Zr, Nb, Mo, or Ta); A is an A-group element (typically Al, Si, P, S, Fe, Cu, Zn, Ga, Ge, As, In, Sn, Sb, Tl, Pb, S); X is C and/or N; and n is any number from 1 to 4.[1,2] After selective removal of A-layer from a parent MAX phase (Ti_3AlC_2), MXene with formula $M_{n+1}X_nT_x$ with T representing the surface terminations arising from the etching process is formed.[3] Due to their rich surface chemistry, unique layered structure, and high electrical conductivity, MXenes have been exciting prospects as functional materials in energy storage applications.[4−6] Yet, a challenge arises from the inherent layer restacking attributed to van der Waals forces.[7,8] This leads to a significant loss of active sites and a diminishing of ionic diffusion channels.[4] Researchers have addressed this issue by intercalating the layers with ions and molecules, forming heterostructures with other 2D materials, building 3D architectures, or combining with carbon-based materials.[7,9−15] Intercalation expands the spaces between MXene sheets, potentially causing spontaneous sheet delamination by weakening the interlayer attractive forces.[16] Gogotsi and co-workers attempted to intercalate various compounds, including hydrazine, thiophene, ethanol, acetone, tetrahydrofuran, formaldehyde, chloroform, toluene, hexane, *N*,*N*-dimethylformamide (DMF), dimethyl sulfoxide (DMSO), and urea into MXene by magnetic stirring.[10] Hydrazine, DMF, DMSO, and urea increased the c-lattice parameter, indicating increased interlayer spacing.

This study sought to advance this concept by employing a polymer (i.e., polyacrylonitrile or PAN) that is soluble in

Received: August 25, 2024
Revised: November 5, 2024
Accepted: November 7, 2024
Published: November 14, 2024

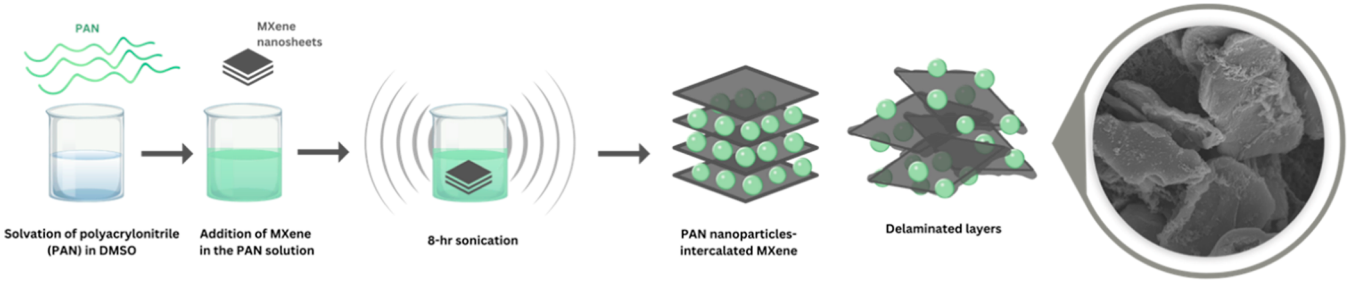

Figure 1. Graphical illustration of the synthesis of PAN intercalation in MXene layers.

DMSO, a solvent already recognized for its intercalation capability in MXene. It was hypothesized that the DMSO-solvated PAN nanoparticles could further expand the interlayer spacing of MXene, inducing delamination, which enhances surface exposure and facilitates more ion channels. While PAN is not traditionally categorized as a conducting polymer, its high dielectric properties make it highly sought after in the energy storage and modern electronics sectors, especially for advancing the trend in electronics toward producing flexible devices like flexible screens, smartphones, and wearable gadgets. By integrating the conductive MXene with PAN, a composite with electrically conducting behavior could be produced based on the principle of percolation.[17] Percolation theory can elucidate the conductive properties of composites comprising conductive fillers and insulating matrices.[18] As the proportion of the conducting material increases, the composite transitions from insulator to conductor. While PAN is primarily referred to as intercalant in this study, it can also be regarded as a polymer matrix with a high percent loading of MXene nanosheet fillers. Compositing an organic material like PAN with a conductive 2D material such as MXene can also enhance structural stability and thus rate performance and cycling stability.[15] Furthermore, employing simple and extended sonication simplifies the composite fabrication process. Combining PAN nanoparticles and MXene nanosheets improved supercapacitance, as revealed by electrochemical assessments.

2. EXPERIMENTAL SECTION

2.1. Materials. Analytical/reagent grade acrylonitrile (Sigma-Aldrich, ≥99%), acetone (Fisher Chemical), 2,2′-azobis (2-methylpropionitrile/AIBN) (Sigma-Aldrich), dimethyl sulfoxide/DMSO (Fisher Chemical), 1-methyl-2-pyrrolidinone/NMP (Alfa Aesar), carbon black (Alfa Aesar), lithium fluoride (Alfa Aesar), poly(vinylidene fluoride)/PVDF (Aldrich), tetraethylammonium tetrafluoroborate/$TEABF_4$ (Thermo Scientific), and acetonitrile (Fisher Chemical) were used without further purification. Carbon cloth (Fuel Cell Earth) was used as a substrate to prepare electrodes. Commercially available MAX phase Ti_3AlC_2 was purchased from Forman, China and was further milled in a planetary mill (SPEX 8000 M Mixer/Mill) using a zirconia Jar and zirconia balls.

2.2. Methods. *2.2.1. Synthesis of MXene.* MXene ($Ti_3C_2T_x$) was prepared by dissolving Ti_3AlC_2 and LiF in 100 mL of 6 M HCl solution, closely following a previous procedure.[19] The solution was magnetically stirred at 400 rpm for 7 days at 70 °C. The crude $Ti_3C_2T_x$ product was collected and centrifuged at 4500 rpm for 10 min. Then, it was washed first with 6 M HCl for 3 cycles and then with DI water. The resultant samples were centrifuged for 15 min until the resulting supernatant reached a pH > 6. The $Ti_3C_2T_x$ product was air-dried in an oven at 75 °C for 24 h before storage.

2.2.2. Synthesis of Polyacrylonitrile. PAN was synthesized via radical polymerization.[20] Briefly, 2 mL of acrylonitrile (monomer), 2 mL of acetone, and 2 mg of AIBN (initiator) were mixed and polymerized at 70 °C with continuous N_2 bubbling. The polymerization reaction took about 2 h and resulted in the formation of a white powder. The product was vacuum-dried for 12 h at room temperature.

2.2.3. Synthesis of MXene-PAN Composite. To prepare the composite, 50 mg of the PAN powder was dissolved in 3.5 mL DMSO. Then, 50 mg of MXene was dispersed into the PAN solution. The mixture was sonicated for 8 h, centrifuged at 8000 rpm for 5 min to separate and remove excess solvent, washed with distilled water thrice, and vacuum-dried at 60 °C for 12 h (Figure 1). The composite was labeled MXene-PAN-DMSO. Two control samples were prepared similarly but only with (1) MXene and DMSO and (2) PAN and DMSO, respectively labeled MXene-DMSO and PAN-DMSO. Having MXene-DMSO as a control was crucial since DMSO is already a known intercalant in MXene.

2.2.4. Preparation of Electrodes. The synthesized materials were used as working electrodes for electrochemical measurements. 5.0 mg of the material was ground and dispersed in 500 μL NMP. Then, 1.0 mg carbon black and 1.0 mg PVDF (binder) were added, and the mixture was sonicated for 1 h. The carbon cloth, used as the substrate for the working electrodes, was pretreated following a previous report.[21] Briefly, 1.5 cm × 1.0 cm pieces of carbon cloth were washed with distilled water, soaked in 100 mL of concentrated HNO_3/H_2SO_4 (1:3% v/v) solution, heated at 60 °C for 2 h, allowed to cool to room temperature, washed with cold distilled water, and finally dried at 60 °C for 6 h. Then, 100 μL of the sonicated working electrode mixture was drop-casted on the pretreated carbon cloth and dried in a vacuum oven at 60 °C for 14 h. To account for the contribution of carbon black and carbon cloth to the electrode's capacitance, a control electrode was also prepared without any active material. A Biologic VMP3 instrument was used to carry out the electrochemical measurements. Ag/AgCl, platinum wire, pretreated carbon cloth, and the synthesized materials served as the reference electrode, counter electrode, substrate, and working electrode, respectively. 1 M $TEABF_4$ in acetonitrile was used as the electrolyte. Impedance spectroscopy, galvanostatic charge−discharge (GCD), and cyclic voltammetry (CV) were included in the electrochemical experiments. eq 1 was used to compute the specific capacitance

$$C_s = \frac{\int_{V_1}^{V_2} \mathrm{Idv}}{2sm\Delta V} \tag{1}$$

where C_s is the specific capacitance (F/g), $\int_{V_1}^{V_2} \mathrm{Idv}$ is the integral CV curve area (AV), s is the scan rate (V/s), m is the mass of the active material (g), and ΔV is the potential window.[22,23]

2.2.5. Asymmetric Device Fabrication. A slurry of electroactive material with PVDF and carbon black was prepared in 5:1:1 weight ratio, coated over a piece of carbon cloth (3 cm × 3 cm), dried at 60 °C for 12 h, and utilized as an active electrode. MXene-PAN-DMSO was used as anode material and carbon black as a cathode material. The device was tested in the potential window of 0.0 to 1.6 V. The active mass loading was 2 mg. For the device assembly, the cathode and the anode were separated by a Whatman 42 filter paper soaked in an electrolyte (1 M $TEABF_4$ in acetonitrile) and pressed by two

https://doi.org/10.1021/acsami.4c14420
ACS Appl. Mater. Interfaces 2024, 16, 64784−64796

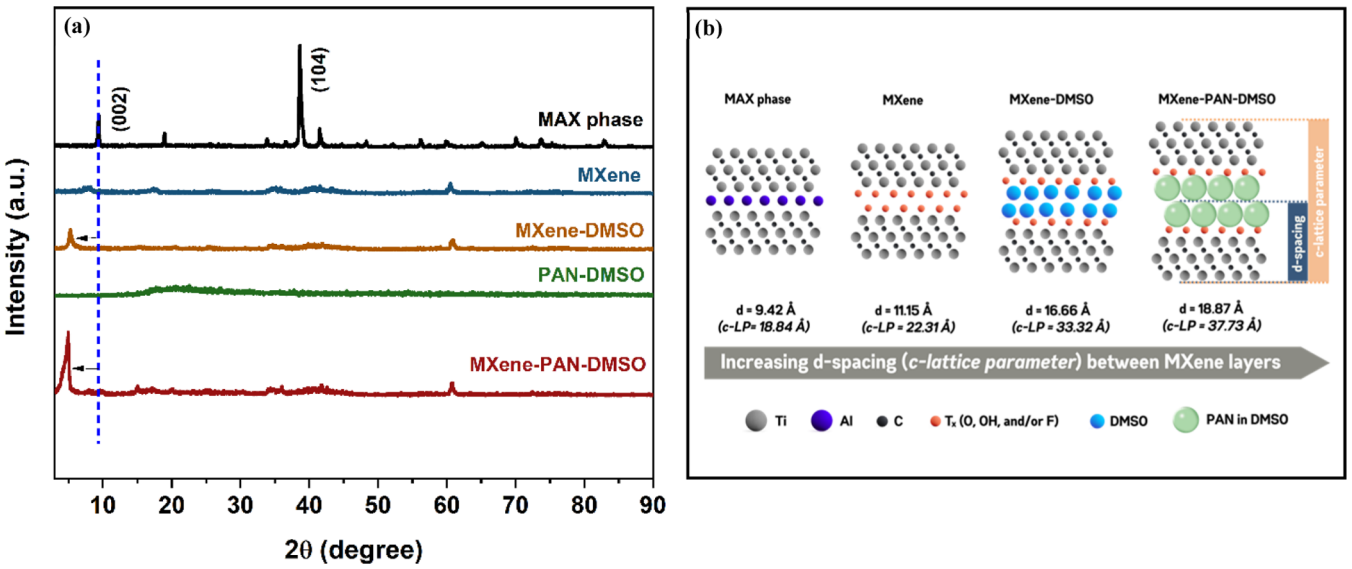

Figure 2. (a) XRD patterns of MAX phase, pristine MXene, MXene-DMSO, PAN-DMSO, and MXene-PAN-DMSO composite; and (b) graphical illustration of the increase in the d-spacing and c-lattice parameter of the MXene layers.

plastic plates. For the device, the specific capacitance (C_s in F/g) was evaluated from GCD plots following eq 2

$$C_s = \frac{2 \times i \times \Delta t}{m\Delta V} \tag{2}$$

where i is charging−discharging current, Δt is the time required for the discharge cycle, m is mass loaded, and ΔV is the voltage range. The energy density (E in W h/kg) and power density (P in W/kg) were evaluated from eqs 3 and 4

$$E = \frac{C\Delta V^2}{7.2} \tag{3}$$

$$P = \frac{E}{\Delta t} \tag{4}$$

2.2.6. Material Characterization. X-ray diffraction (XRD) was used to examine the crystal structure of the nanocomposites. A Rigaku MiniFlex 600 diffractometer fitted with a scintillation counter detector and a Cu K_α radiation source was utilized. At 40 kV and 15 mA, XRD patterns were recorded at intervals of 10 to 60° (0.02° step, 2°/min speed). To calculate the d-spacing and c-lattice parameters, Bragg's law was used

$$d = \frac{n\lambda}{2\sin\theta} \tag{5}$$

$$c - \mathrm{LP} = 2\mathrm{d} \tag{6}$$

where d is the d-spacing or interplanar distance, λ is the X-ray wavelength, n is the order of reflection, θ is the Bragg's angle in radians, and c−LP is the c-lattice parameter.

A Horiba XploRA Raman confocal microscope was used to study the vibrational energy modes of the samples. The laser power, grating, and slit were 532 nm, 1800T, and 100 respectively. Solid powder samples were directly anayzed after calibrating the instrument using a standard silicon wafer slide. To gather X-ray photoelectron spectra (XPS), an ESCALABTM XI + XPS with 500 nm laser power was utilized. The energy step size and dwell time were 0.1 eV and 50 ms, respectively. Samples were prepared in atmospheric conditions in a HEPA-filter fitted Laminar flow chamber and deposited, using a spatula, on a substrate attached to a stainless steel sample holder. The surface area was determined using a Micromeritics 3Flex analyzer with N_2 as the analysis adsorptive. To study their morphology, the samples were examined using a JEOL JSM-IT800 Schottky field emission scanning electron microscope (FE-SEM). The samples were dispersed in ethanol and deposited on a silicon wafer. The high-resolution transmission electron microscopy (HR-TEM) operated at an accelerating voltage of 200 kV from JEOL 2100PLUS with a STEM/EDS capability was used to examine the morphology and crystallinity of the composite.

3. RESULTS AND DISCUSSION

The expansion of MXene layers by intercalating cations (e.g., K^+, Na^+, NH_4^+) and large organic molecules (e.g., DMSO, isopropyl amine, urea, bacterial cellulose) has been demonstrated in literature.[24−26] Acting as spacers, these cations and molecules facilitate the delamination of the stacked sheets by weakening the interlayer interactions, especially upon sonication.[25] This work has demonstrated the possibility of expanding the interlayer spacing in MXene even more by using a DMSO-soluble polymer. One viable polymer choice is polyacrylonitrile (PAN), whose overall solubility parameter (25.3 $MPa^{1/2}$) is comparable to that of DMSO (26.6 $MPa^{1/2}$).[27] The DMSO solvent molecules penetrate the PAN polymer molecules by breaking up the polar−polar interactions of neighboring nitrile groups and subsequently forming solvent bridges in their place.[27] Figure S1 displays SEM images of PAN in DMSO, showing the formation of nanoparticles after 8 h of sonication. Moreover, the nitrile functional group in PAN that repeats in its polymeric chain could help in forming strong interactions with the surface termination groups in MXene. The nitrile group works as a hydrogen bonding acceptor because of the lone pair of electrons on the nitrogen atom and a significant dipole moment between the electron-rich nitrogen atom and the electron-deficient carbon atom. This could be utilized to achieve a reasonably strong, attractive interaction between PAN and MXene. The successful loading of PAN onto the MXene surface could be inferred from the XRD, Raman spectroscopy, XPS analyses. Primarily, the XRD results and calculations using eqs 5 and 6 demonstrated a significant increase in the interlayer spacing of the MXene sheets upon intercalation with DMSO and PAN-DMSO. In Figure 2a, the diffraction peak of MAX phase at 2θ of 9.38° related to the (002) plane shifted to lower angles and broadened, indicating that the c-lattice parameter (c−LP) increased in MXene,

https://doi.org/10.1021/acsami.4c14420
ACS Appl. Mater. Interfaces 2024, 16, 64784−64796

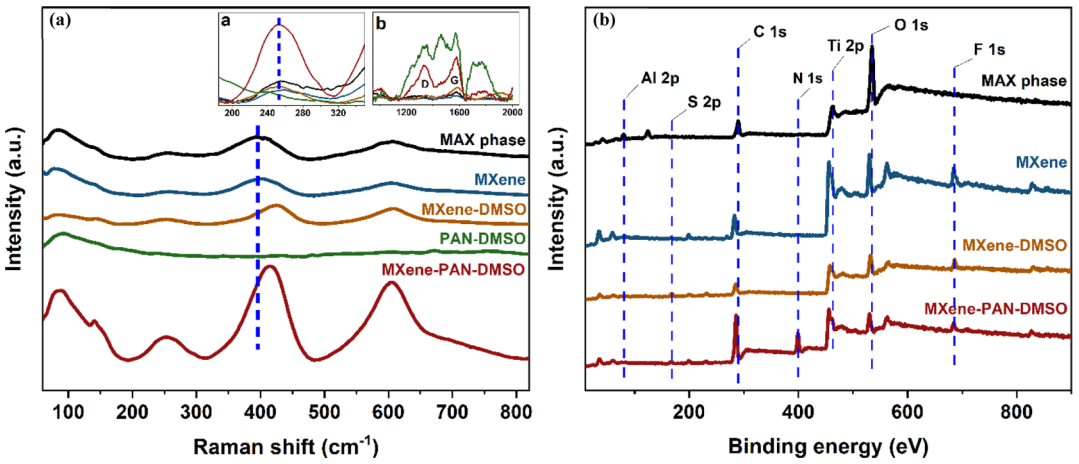

Figure 3. (a) Raman spectra of MAX phase, pristine MXene, MXene-DMSO, PAN-DMSO, and MXene-PAN-DMSO composite; (b) XPS survey spectra of MAX phase, pristine MXene, MXene-DMSO, and MXene-PAN-DMSO composite. Inset: (a) Emphasis on the peak shift observed at ~255 cm^{-1} and (b) Raman spectra of all samples at the range ~1000−2000 cm^{-1} where the D and G bands are located.

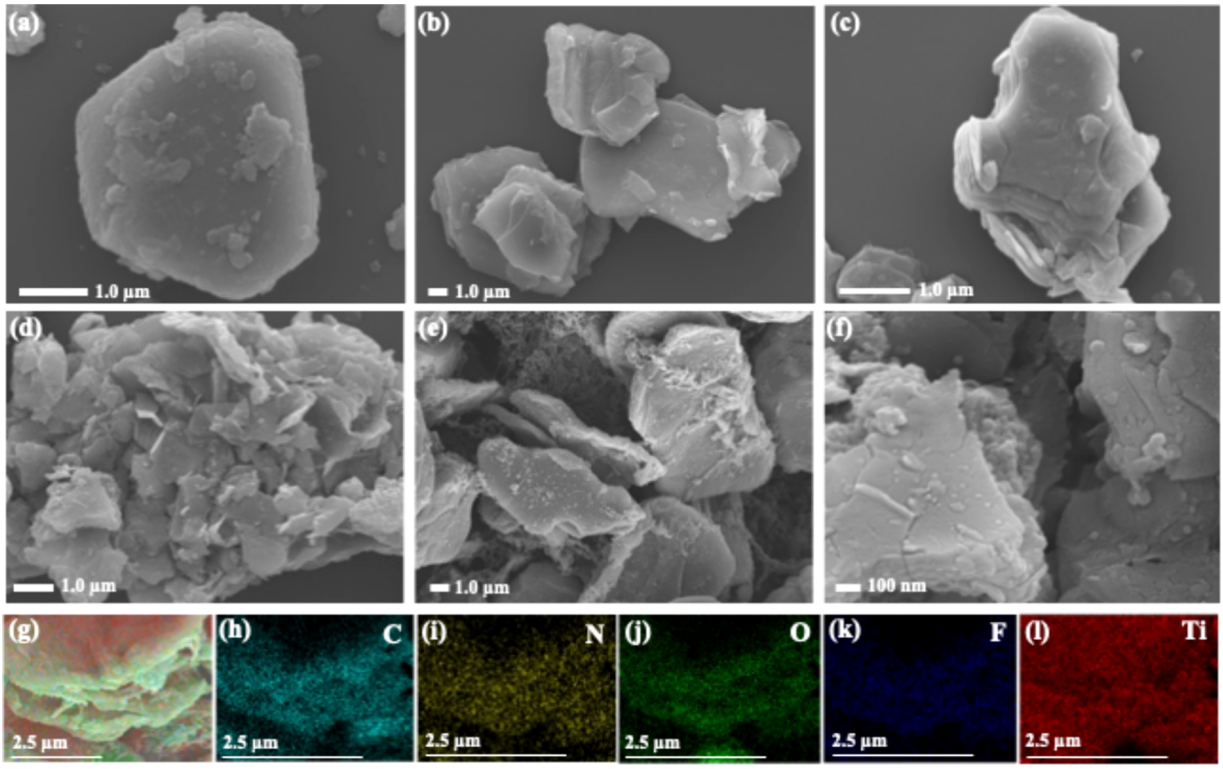

Figure 4. SEM images of (a) MAX phase, (b) pristine MXene, (c) MXene-DMSO, all displaying stacked layers; (d−f) MXene-PAN-DMSO composite, showing more delaminated layers and an increased exposed surface area due to the intercalation of PAN, and (g−l) EDX elemental mapping of the MXene-PAN-DMSO composite, displaying a good distribution of N throughout the structure which indicates the successful loading of PAN in the composite.

MXene-DMSO, and MXene-PAN-DMSO.[6] The c−LP for 2D materials, like MXene, provides information on the distance between parallel adjacent sheets. Therefore, changes in the c−LP can be monitored to assess the success of intercalation.[28] The disappearance of the most prominent peak at ~40°, corresponding to the (004) plane, signaled the effective removal of the aluminum layer from the MAX phase.[28] This selective etching of aluminum led to the formation of a highly active surface that readily interacted with surrounding species, particularly those present in the etching solution, to minimize surface energy. The LiF/HCl etchant generated an HF-containing aqueous solution, resulting in −F, −OH, and/or = O termination groups on the exposed MXene surface.[29] These groups increased the c−LP of MXene to 22.31 Å from 18.84 Å of the MAX phase. Upon sonication with DMSO and PAN-DMSO, the c−LP further increased to 33.32 and 37.73 Å, respectively. This is visually represented in Figure 2b.

The Raman spectra of all samples, excluding the PAN-DMSO control, displayed features in the 100−800 cm^{-1} range (Figure 3a). The spectrum of the parent MAX phase was comparable to that of the MXene and MXene-containing samples when a 532 nm laser was used, which is similarly

https://doi.org/10.1021/acsami.4c14420
ACS Appl. Mater. Interfaces 2024, 16, 64784−64796

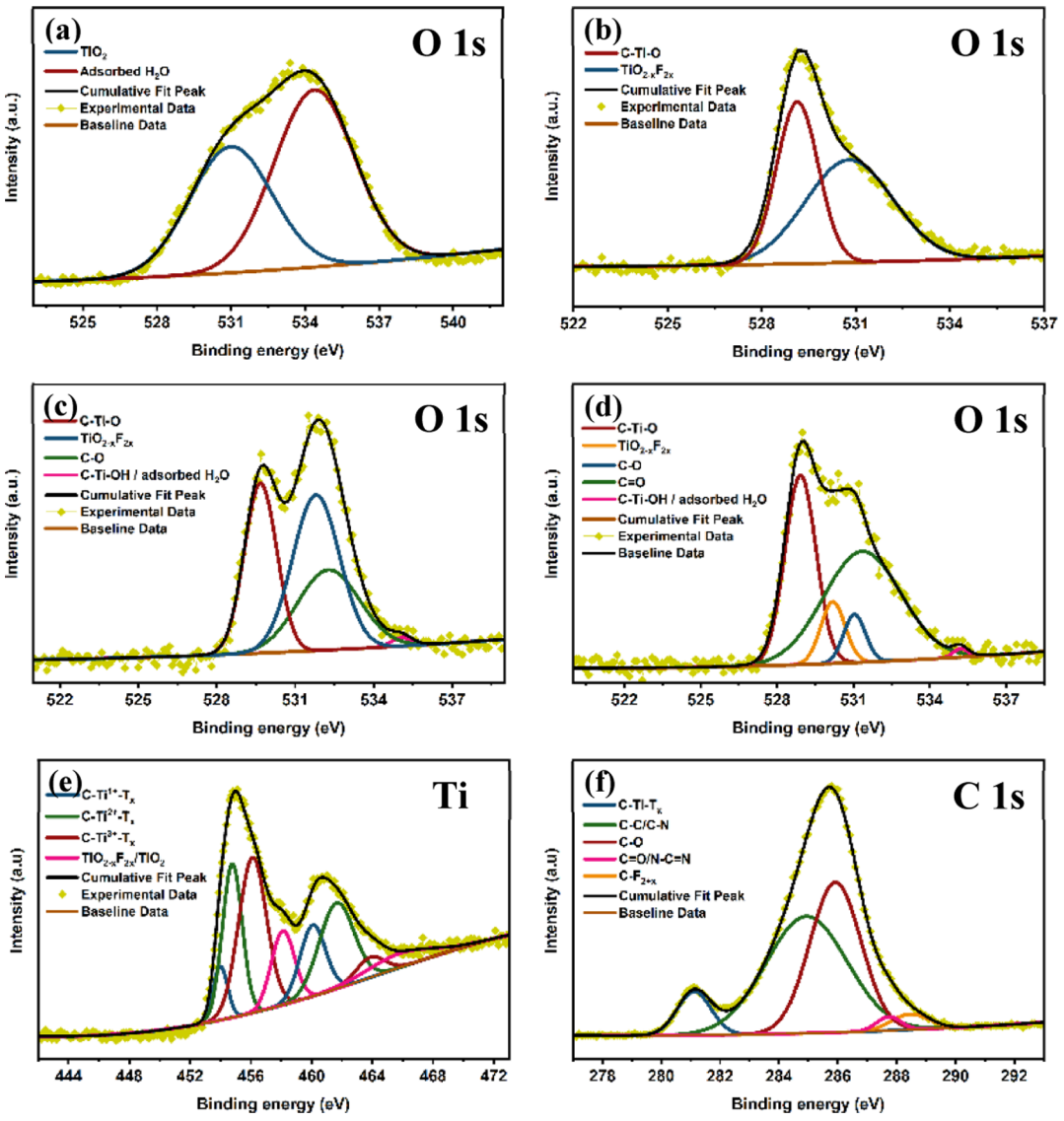

Figure 5. High-resolution component peak fittings of (a) O 1s for MAX phase, (b) O 1s for pristine MXene, (c) O 1s for MXene-DMSO, (d–f) O 1s, Ti 2p, and C 1s for MXene-PAN-DMSO composite, respectively.

observed in previous studies.[29−31] The basic Raman modes of the MAX phase were retained, indicating that the hexagonal crystal structure was preserved,[30] but with unit cell distortions as indicated by peak shifting (emphasized by the broken lines and inset a) in the spectrum.[32] This is due to surface termination groups, intercalants, and any adsorbed species in MXene affecting its lattice vibrations.[32] The characteristic peaks at ∼255 ∼400, and ∼605 corresponded to the in-plane vibrations of carbon and oxygen bonds and Ti−C vibrations, respectively.[31] Although oxygen atoms are not inherently present in the MAX phase, exposure to air and the laser irradiation during Raman analysis caused the formation of oxides[32,33] (which was also confirmed in the succeeding XPS result in a later section). Interestingly, the Raman intensity of MXene-PAN-DMSO was distinctively higher than the rest of the samples. This could be explained by the delamination and random orientation of the sheets, which could also be seen in its SEM (Figure 4d–f) images. There was a decreased coupling between flakes. Thus, the surface group vibrations were stronger, resulting in highly pronounced Raman peaks.[32] On the other hand, the peak intensities of the MAX phase, MXene, and MXene-DMSO were comparable because the restacking of the MXene sheets had a similar orientation as that of the parent MAX phase.[32] This was also observed in their corresponding SEM images (Figure 4a–c). These images clearly showed that the nanostructure surface of the composite was altered, resulting in increased surface area. This was further validated by N_2 adsorption/desorption analysis, which revealed a 127.8% increase in surface area for the composite, measured at 19.7 m^2/g, compared to 8.65 m^2/g for pristine MXene (Figure S2). This surface modification is beneficial for improving the reactivity of active sites by changing surface structural characteristics and electronic configurations.[34−36]

Furthermore, only the MXene-PAN-DMSO composite showed prominent D (∼1335 cm^{-1}) and G (∼1580 cm^{-1}) bands, which represent disorder-induced lattice vibrations and ordered sp^2 hybridized carbon structures, respectively[31,37] (inset b in Figure 3a). The D and G intensities (I_D/I_G) ratio was 0.77, indicating that the composite has a higher degree of structural order and fewer defects in its carbon lattice. A broad peak in this range in the PAN-DMSO control indicates that the

https://doi.org/10.1021/acsami.4c14420
ACS Appl. Mater. Interfaces 2024, 16, 64784−64796

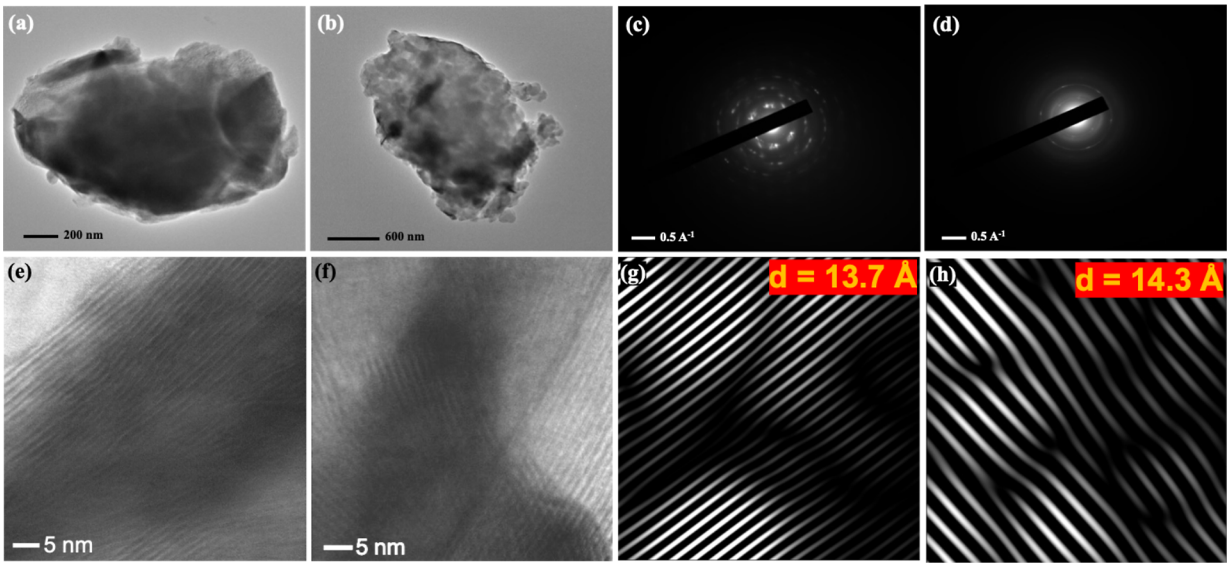

Figure 6. (a) TEM image, (c) SAED pattern, (e) HR-TEM image, and (g) lattice fringe of MXene-DMSO; (b) TEM image, (d) SAED pattern, (f) HR-TEM image, and (h) lattice fringe of MXene-PAN-DMSO composite.

graphitic carbon observed in the MXene-PAN-DMSO composite can be attributed to the addition of PAN.

Realistically, the MXene synthesis process results in a random mix of surface groups that are nonuniformly distributed across the entire sheet.[29] Literature has shown that achieving MXenes with homogeneous surface terminations is quite challenging.[38,39] The complexity of the surface also leads to inconsistent interpretations of XPS results in published works.[29] Nonetheless, XPS can provide helpful information on the elemental composition of MXenes. Figure 3b shows the XPS survey spectra of the samples, and individual spectra are in Figure S3 for emphasis. A few observations from the elemental survey are noteworthy: (1) the presence of Al 2p peak exclusively in the MAX phase corroborated the XRD finding of successful etching of the Al layer; (2) the detection of F 1s in MXene, MXene-DMSO, and MXene-PAN-DMSO confirmed surface termination of F groups upon Al etching; (3) the presence of S 2p in MXene-DMSO and MXene-PAN-DMSO indicated the successful intercalation of DMSO between MXene layers; (4) the presence of N 1s in MXene-PAN-DMSO confirmed PAN intercalation; and (5) shifts in the binding energy of C 1s, Ti 2p, and O 1s indicated variations in the chemical environment of these atoms among the samples. For instance, the deconvoluted O 1s peaks (Figure 5a–d) exhibit evident differences in their component peaks. The MXene-PAN-DMSO composite showed the most complex spectrum, displaying peaks at 528.9, 530.2, 531.0, 531.4, and 535.2 eV, which can be assigned to C–Ti–O, $TiO_{2-x}F_{2x}$, C–O, C═O, and C–Ti–OH or adsorbed H_2O, respectively.[33] The Ti 2p and C 1s spectra for the MXene-PAN-DMSO composite are also shown (Figure 5e–f). The Ti 2p spectrum displays two main peaks at ∼455 and ∼461 eV, corresponding Ti $2p_{3/2}$ and Ti $2p_{1/2}$, respectively.[33,40] The deconvolution revealed distinct Ti bonding environments (C–Ti^{n+}–T_x, $TiO_{2-x}F_{2x}$, TiO_2).[33] The peaks in the resolved C 1s spectrum observed at 280–290 eV represented various carbon bonds such as C–Ti–T_x, C–C, C–N, C–O, C═O, and C–F_{2x}.[33,41,42]

The TEM images of the MXene-DMSO and the MXene-PAN-DMSO composite were taken for comparison (Figure 6). MXene-DMSO exhibited darker regions, indicative of a more stacked-layer structure (Figure 6a). In contrast, the composite displayed the presence of particles covering and/or intercalating the layers, confirming the presence of PAN (Figure 6b). The selected area electron diffraction (SAED) images further supported these findings. The SAED pattern of MXene-DMSO (Figure 6c) showed higher crystallinity compared to that of MXene-PAN-DMSO (Figure 6d), which can be explained by the amorphous nature of the PAN polymer. Moreover, the high-resolution TEM images revealed larger lattice d-spacing for the MXene-PAN-DMSO composite, measured at 14.3 Å (Figure 6f,h), compared to the 13.7 Å measured for MXene-DMSO (Figure 6e,g). The TEM elemental mapping (Figure S4) also showed the formation of a MXene-PAN composite.

Electrochemical tests were conducted using 1 M $TEABF_4$ in acetonitrile as the electrolyte to assess the supercapacitor performance of the material. Using an organic electrolyte allowed for a wide potential window, avoiding interference from water electrolysis that would occur if an aqueous electrolyte was used.[43,44] In Figure 7a, the comparative cyclic voltammetry (CV) curves, recorded at a scan rate of 100 mV/s within a potential range of −1.15 to 0 V, illustrate that the MXene-PAN-DMSO composite exhibited the largest area, suggesting the highest capacitance among all the samples. It also consistently showed the highest capacitance across all scan rates, with the corresponding CV curves in Figure S5. The MXene-PAN-DMSO composite could accommodate a current density up to ∼2.3 A/g at 100 mV/s (Figure 7a), equivalent to a substantial increase of 199%, 46%, and 36% from the parent MAX phase, pristine MXene, and MXene-DMSO, respectively. MXene-DMSO and MXene-PAN-DMSO exhibited comparable CV shapes, featuring a pair of redox peaks indicative of Faradaic reactions. The redox peaks were not as defined in the pristine MXene, a common observation in multilayer $Ti_3C_2T_x$ MXene supercapacitors.[5,43] The more pronounced redox peaks at about −0.8 and −0.7 V for the MXene-PAN-DMSO composite indicated the efficient intercalation/deintercalation of TEA^+ ions within the expanded MXene layers.[44] As shown in Figure 7c, both the MXene-DMSO and MXene-PAN-DMSO composites exhibited improved capacitance relative to

https://doi.org/10.1021/acsami.4c14420
ACS Appl. Mater. Interfaces 2024, 16, 64784−64796

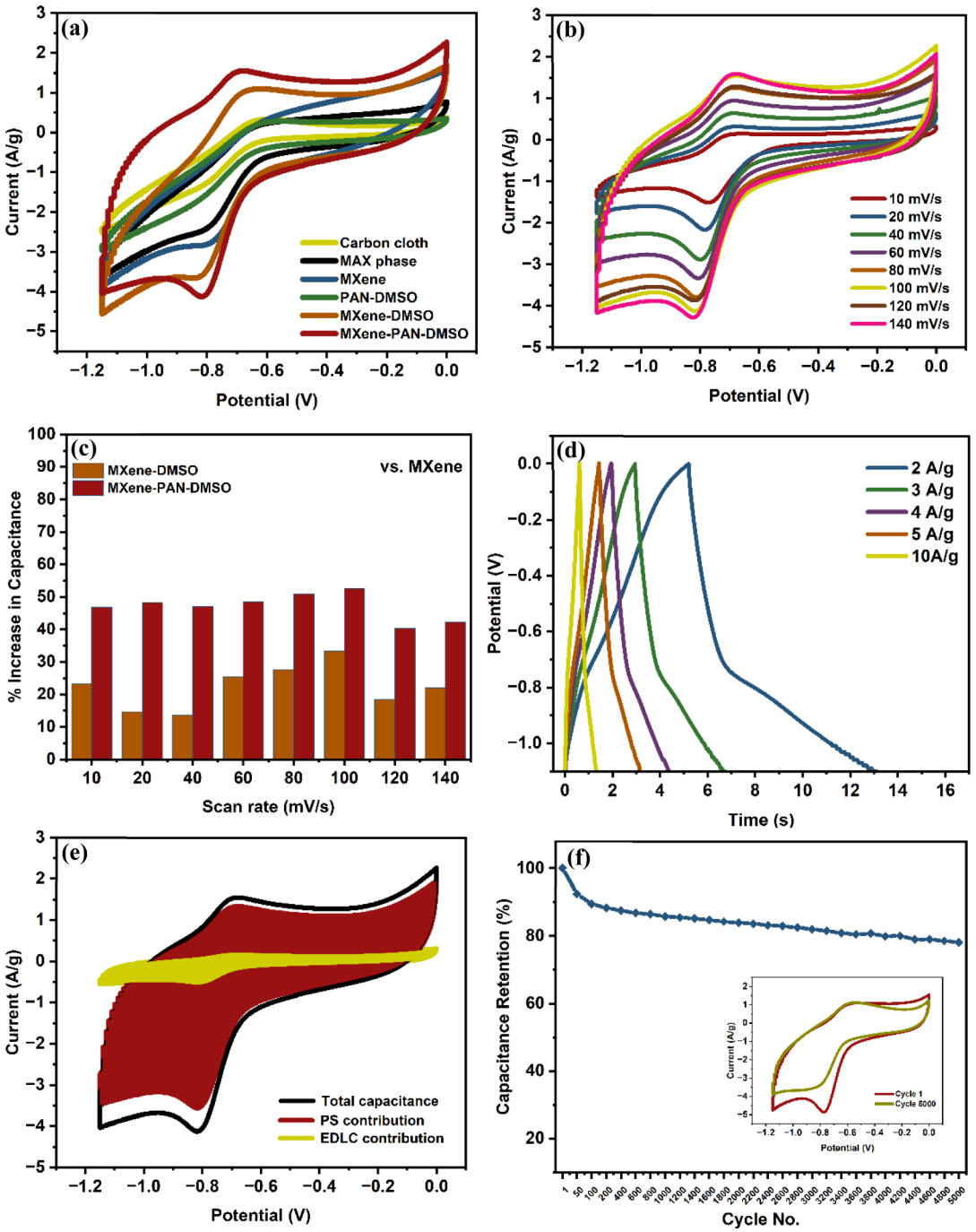

Figure 7. (a) Comparative cyclic voltammetry (CV) curves of all samples at 100 mV/s, (b) CV curves of the MXene-PAN-DMSO composite at different scan rates from 10 to 140 mV/s, (c) Increase in the specific capacitance of MXene-DMSO and MXene-PAN-DMSO relative to pristine MXene, (d) Galvanostatic charge and discharge (GCD) curves of MXene-PAN-DMSO composite at different current densities, (e) Pseudocapacitive and EDLC contributions to the capacitance of the MXene-PAN-DMSO composite, and (f) CV cycling stability of the MXene-PAN-DMSO composite at 140 mV/s.

pristine MXene across all measured scan rates, with the MXene-PAN-DMSO composite showing greater enhancement. For instance, the MXene-PAN-DMSO composite increased the capacitance of pristine MXene by 48.3% at a scan rate of 20 mV/s, compared to a 14.7% increase for MXene-DMSO. Figure 7d shows the galvanostatic charge and discharge (GCD) curves of the MXene-PAN-DMSO composite at various current densities (2.0, 3.0, 4.0, 5.0, 10 A/g). Similar to cyclic voltammetry, GCD data directly correlate with capacitive charge.[45] Interestingly, only the MXene-PAN-DMSO composite could sustain the wide potential window of −1.15 to 0 V (the same potential window used in the CV tests) during the GCD tests. For all other samples, the window was narrowed to −0.7 to 0 V (Figure S6).

The MXene-PAN-DMSO composite exhibited a specific capacitance of 24.1 F/g at a scan rate of 10 mV/s. This value was 30.8% higher than MXene-DMSO (16.7 F/g), 46.9% higher than the pristine MXene (12.8 F/g), and 72.2% higher than the parent MAX phase (6.7 F/g). A similar trend was observed in the GCD-derived capacitances. The improvement

https://doi.org/10.1021/acsami.4c14420
ACS Appl. Mater. Interfaces 2024, 16, 64784−64796

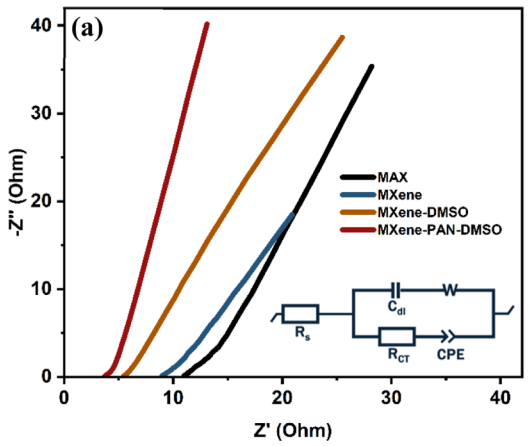

(b)

	Solution resistance, R_S (Ω)	Charge transfer resistance, R_{CT} (Ω)	Diffuse layer resistance (Ω)
MAX phase	10.95	4.48	17.13
MXene	8.88	3.10	11.81
MXene-DMSO	5.38	1.77	19.98
MXene-PAN-DMSO	3.66	1.93	9.36

	Conductivity (S/m)	Sheet resistance (Ω/square)
MAX phase	2426	4.12
MXene	2701	3.70
MXene-DMSO	3617	2.76
MXene-PAN-DMSO	7322	1.37

Figure 8. (a) Nyquist plots with equivalent circuit and (b) summary table of the results from the EIS study and four-point probe test.

in the capacitance of the composite could be attributed to the enhanced accessibility of the MXene sheets due to the increased interlayer spacing, as revealed in the XRD results.[43] This allowed for more efficient ion transport during charge and discharge. In fact, the rising trend in the specific capacitance among the samples ($C_{s,MAX}$ < $C_{s,MXene}$ < $C_{s,MXene\text{-}DMSO}$ < $C_sC_{,MXene\text{-}PAN\text{-}DMSO}$) just mirrored the increasing trend in the c-lattice parameter (c−LP_{MAX} < c−LP_{MXene} < c−$LP_{MXene\text{-}DMSO}$ < c−$LP_{MXene\text{-}PAN\text{-}DMSO}$). One interesting observation was that, at a narrow range of scan rates (60−100 mV/s), the capacitance of MXene-PAN-DMSO remained relatively constant instead of the typical decline in capacitance as the scan rate increases.[23,46] The reduced dependence of capacitance to the scan rate had been previously observed in another study and was attributed to the larger interlayer spacing, which better facilitated ion movement.[5] However, considering a more comprehensive range of scan rates (10−140 mV/s), the expected inverse linear relationship was still observed for the composite. This can be deduced from Figure S7a which shows C vs $s^{-1/2}$. Typically, as the scan rate increases, the redox reactions happen faster, leading to shorter time intervals for ions to penetrate and diffuse to and from the electrode material.[47,48] This reduces charge storage capacity, as the ions have less time to accumulate and participate in Faradaic or double-layer charge storage processes. Moreover, the evident difference in the D and G regions (around 1200−1600 cm^{-1}) in the Raman spectra of the PAN-DMSO control and MXene-PAN-DMSO composite, as depicted in Figure 3a inset b, clearly indicated a notable alteration in the carbon structure of PAN in the composite. It is possible that the presence of MXene substantially reduced the temperature required for the aromatization of PAN, a process that might have occurred during the 8 h sonication at mild heat (~80 °C).[49] If indeed the case, the cyclization of the nitrile groups might have aided in electron transport during charge and discharge cycles. However, this assumption requires further investigation and is not the primary focus of this study. The deconvoluted N 1s XPS spectrum for MXene-PAN-DMSO is shown in Figure S8.

Trasatti plots for the MXene-PAN-DMSO composite are presented in Figure S7 to study the capacitive contributions from surface-controlled (electrical double layer/EDL capacitance) and diffusion-controlled (pseudocapacitance).[50,51] Because the access of electrolyte ions is restricted only to the outer surface of the electrode material at high scan rates (s), the capacitance (C) is mainly dependent on the outer surface and electrolyte interaction.[51] The y-intercept then of the linear fit of $s^{-1/2}$ vs C gives the capacitive contribution from the EDL (C_{EDL}).[51,52] Conversely, at low scan rates, diffusion-controlled processes dominate, allowing electrolyte ions to have practically unrestricted access to both the inner and outer surfaces of the electrode material.[51] Here, the y-intercept of the linear fit of $s^{1/2}$ vs C^{-1} gives the total capacitance ($1/C_T$).[51,52] The difference between C_T and C_{EDL} gives the pseudocapacitive contribution (C_{PS}). From these, it was observed that the MXene-PAN-DMSO composite showed a combination of surface-controlled and diffusion-controlled charge-storage mechanisms, contributing 13.7% (C_{EDL}) and 86.3% (C_{PS}) to the capacitance, respectively (Figure 7e). The dominance of C_{PS} was consistent with the shape of the GCD curve (Figure 7d), where a significant decrease in the potential at the beginning of the discharge process indicated pseudocapacitive behavior.[53] Furthermore, as shown in Figure 7f, the composite exhibited CV cycling stability with 78.1% capacitance retention after 5000 cycles, even at a fast scan rate of 140 mV/s.

Electrochemical impedance spectroscopy (EIS) is another technique based on the disturbance of an electrochemical system in equilibrium by applying a sinusoidal signal across a broad spectrum of frequencies and recording the system's corresponding sinusoidal response.[54] From this, a Nyquist plot can be obtained, presenting the imaginary part of the impedance as a function of the real part. Physical meanings are assigned to the graph elements, such as charge-transfer resistance, internal resistance, and diffusion impedance.[45,55] A Nyquist plot provides insight into the different resistive and capacitive behaviors of a material and the corresponding fitted equivalent circuit can be used to model the electrochemical behavior of a supercapacitor, providing a deeper understanding of its internal processes. To accurately match the experimental data, both pseudocapacitive and EDL charge-storage mechanisms must be accounted for in the circuit model.[56] Figure 8a displays the Nyquist plot of the samples recorded at an open circuit potential and frequency range of 1 Hz−100 kHz. In electrochemical systems, the Nyquist plot pattern typically comprises a semicircle, which indicates impedance from charge transfer-controlled electrochemical processes (faradaic), and a straight line, indicating impedance from mass transfer-controlled electrochemical processes (nonfaradaic).[54] In the faradaic pathway, the current crosses the interface via the reduction and oxidation of active species on the electrode.[57] In the nonfaradaic pathway, the charged particles from the

https://doi.org/10.1021/acsami.4c14420
ACS Appl. Mater. Interfaces 2024, 16, 64784−64796

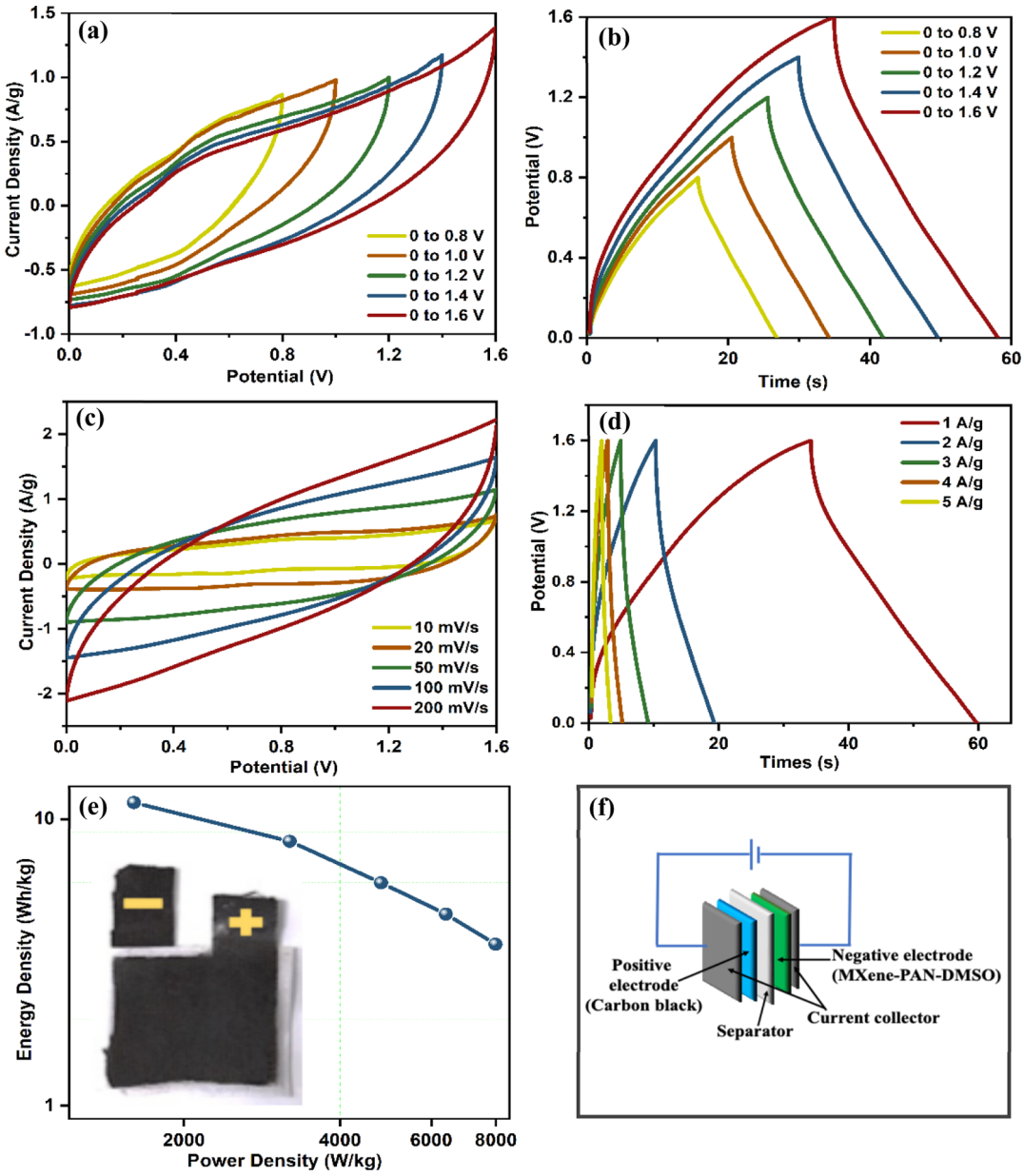

Figure 9. Electrochemical performance of asymmetric device: (a) CV curves with increasing potential window, (b) GCD profiles with increasing potential window, (c) CV curves at different scan rates, (d) GCD profiles at different current densities, (e) Ragone plot, inset: digital photograph of the assembled asymmetric device, and (f) schematic diagram of the assembled device.

electrolyte do not cross the electrode−electrolyte interface. The current is carried by the charging and discharging the electric double layer.[57] Moreover, the semicircle indicates a transmissive boundary on the electrode, allowing diffusing species from the electrolyte to permeate in the electrode.[54,58] The less evident semicircle in the EIS curves of the prepared electrodes suggested a very low charge transfer resistance (R_{CT}) in the electrode−electrolyte interface.[40,59,60] This was confirmed by the values obtained from fitting the curve in an equivalent circuit (Figure 8b). The summary table also includes Supporting Information for conductivity and sheet resistance which were obtained from a four-point probe meter. Over time, when the finite diffusion region becomes impermeable, charge transfer is halted and a subsequent straight line appears, indicating a reflective boundary mass transfer impedance.[54,58] The MXene-PAN-DMSO composite showed the steepest line, indicating the best capacitive behavior and the lowest diffuse-layer resistance.[54,58,61] From these data, it was evident that the MXene-PAN-DMSO composite had the best overall performance with solution resistance (R_s) of 3.66 Ω, R_{CT} of 1.93 Ω, diffuse-layer resistance of 9.36 Ω, conductivity of 7322 S/m, and sheet resistance of 1.37 Ω/square.

The practical application of MXene-PAN-DMSO composite was studied by examining the electrochemical performance of the assembled asymmetric device in a two-electrode setup. The composite was used as the negative electrode, given that MXene has proven to be an effective anodic material for asymmetric devices.[61,62] MXenes are more stable at negative potentials, where they are less likely to undergo oxidation and material degradation. Figure 9f depicts the components of the device. The working potential of the device was estimated by

https://doi.org/10.1021/acsami.4c14420
ACS Appl. Mater. Interfaces 2024, 16, 64784−64796

conducting CV and GCD scans with increasing potential limits, shown in Figure 9a and b, respectively. After evaluating these electrochemical performances, the working potential was set to 1.6 V. The CV profiles of the device with increasing scan rates are shown in Figure 9c, revealing a pseudocapacitance at lower scan rates due to the reversible redox state of Ti in MXene. Furthermore, the respective GCD profiles (Figure 9d) at different current densities well complement the CV curve nature of the device.

The specific capacitance, energy density, and power density of the assembled asymmetric device were determined with changing current densities. The device exhibited a good performance, delivering a specific capacitance of 32.1 F/g, an energy density of 11.42 W h/kg, and a power density of 1599.7 W/kg at 1 A/g. The findings are summarized in Table 1. The

Table 1. Performance of the Assembled Asymmetric Device from MXene-PAN-DMSO Nanocomposite at Varying Current Densities

current density (A/g)	specific capacitance (F/g)	Energy density (W h/kg)	power density (W/kg)
1	32.1	11.42	1599.7
2	23.3	8.37	3198.7
3	16.2	5.99	4802.7
4	12.8	4.66	6403.0
5	10.1	3.66	7985.5

Ragone plot (Figure 9e) demonstrated the device's good rate capability. Finally, the stability test showed that the device retained 82.2% of its capacitance after 10,000 cycles (Figure 10a), with a slight increase in solution resistance from 8.9 to 14.1 Ω and diffuse-layer resistance from 100.7 to 130.9 Ω, as revealed by the EIS study (Figure 10b). Compared to various MXene-based supercapacitors from literature, the MXene-PAN-DMSO device showed a comparable performance (Table S1).

4. CONCLUSION

In this work, a composite consisting of MXene and PAN was successfully synthesized and assessed for supercapacitor applications using electrochemical tests. MXene ($Ti_3C_2T_x$) was derived from its parent MAX phase (Ti_3AlC_2) using LiF/HCl as an etchant to remove aluminum, while PAN was synthesized via radical polymerization. The MXene-PAN composite was subsequently produced using a straightforward sonication technique. Utilizing a solvent (DMSO) that solubilizes PAN but disperses MXene, the PAN nanoparticles were effectively intercalated into the interlayer spaces of MXene sheets, causing subsequent delamination of the layers. X-ray diffraction analysis showed an increase in the c-lattice parameter from 22.31 Å for the pristine MXene to 37.73 Å for the MXene-PAN composite, indicating an expanded interlayer spacing between the multilayer MXene sheets. This intercalation of PAN nanoparticles and the resulting increase in interlayer gaps proved beneficial in preventing MXene sheet restacking, thereby exposing more surface area, which is crucial for energy storage applications. The rising trend in the specific capacitance (C_s) among the samples ($C_{s,MAX} < C_{s,MXene} < C_{s,MXene\text{-}DMSO} < C_{s,MXene\text{-}PAN\text{-}DMSO}$) just mirrored the increasing trend in the c-lattice parameter ($c{-}LP_{MAX} < c{-}LP_{MXene} < c{-}LP_{MXene\text{-}DMSO} < c{-}LP_{MXene\text{-}PAN\text{-}DMSO}$). Electrochemical tests showed that the composite had the best performance in capacitance, resistance, and conductivity. The assembled asymmetric device delivered a good specific capacitance of 32.1 F/g and an energy density of 11.42 W h/kg, demonstrating the practical application of the MXene-PAN composite.

■ ASSOCIATED CONTENT

Supporting Information

The Supporting Information is available free of charge at https://pubs.acs.org/doi/10.1021/acsami.4c14420.

SEM images of the PAN nanoparticles in DMSO; N_2 adsorption/desorption isotherms for pristine MXene and MXene-PAN-DMSO; Al 2p, S 2p, C 1s, N 1s, Ti 2p, O 1s, and F 1s XPS spectra of MAX phase, pristine MXene, MXene-DMSO, and MXene-PAN-DMSO composite; TEM image of MXene-PAN-DMSO composite, corresponding EDX overlay elemental map, and individual elemental mapping for C, Cl, F, N, O, S, and Ti; cyclic voltammetry curves at different scan rates from 10 to 140 mV/s of carbon cloth with carbon black and PVDF, MAX phase, pristine Mxene, MXene-DMSO, PAN-DMSO, and MXene-PAN-DMSO; Galvanostatic charge and discharge (GCD) curves of MAX phase, MXene, MXene-DMSO, and PAN-DMSO; Linear fit of scan rate vs capacitance ($s^{-1/2}$ vs C) and linear fit of $s^{1/2}$ vs 1/C; high-resolution component peak fittings of N 1s for MXene-PAN-DMSO composite; comparative performance of various MXene-based supercapacitor devices (PDF)

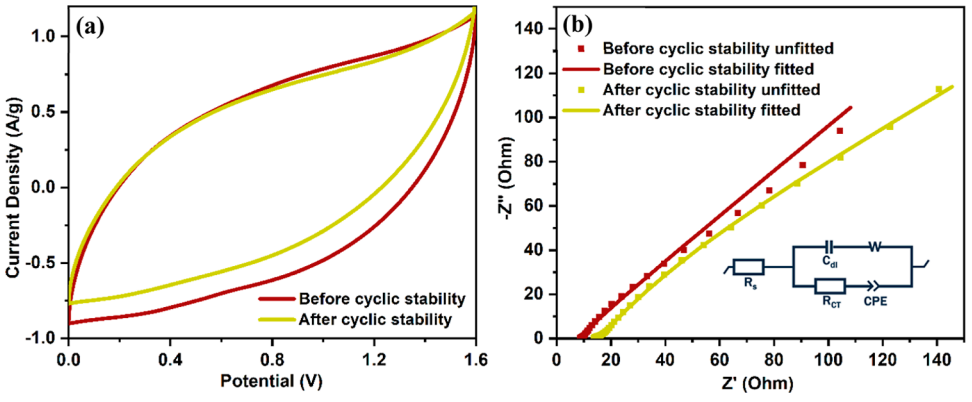

Figure 10. (a) CV curves at 50 mV/s, (b) Nyquist plots of the asymmetric device before and after 10,000 cycles, and inset b: fitted circuit.

https://doi.org/10.1021/acsami.4c14420
ACS Appl. Mater. Interfaces 2024, 16, 64784−64796

AUTHOR INFORMATION

Corresponding Author

Bishnu Prasad Bastakoti − *Department of Chemistry, North Carolina A&T State University, Greensboro, North Carolina 27411, United States;* orcid.org/0000-0002-4651-7393; Email: bpbastakoti@ncat.edu

Authors

Shanna Marie M. Alonzo − *Department of Chemistry, North Carolina A&T State University, Greensboro, North Carolina 27411, United States*

Shrabani De − *Department of Chemistry, North Carolina A&T State University, Greensboro, North Carolina 27411, United States*

Vanessa Morris − *Department of Chemistry, Physics, and Materials Science, Fayetteville State University, Fayetteville, North Carolina 28301, United States*

Daniel E. Autrey − *Department of Chemistry, Physics, and Materials Science, Fayetteville State University, Fayetteville, North Carolina 28301, United States;* orcid.org/0000-0002-8008-5248

Bhoj Raj Gautam − *Department of Chemistry, Physics, and Materials Science, Fayetteville State University, Fayetteville, North Carolina 28301, United States*

Gayani Pathiraja − *Department of Nanoscience, Joint School of Nanoscience and Nanoengineering, University of North Carolina at Greensboro, Greensboro, North Carolina 27401, United States*

Complete contact information is available at: https://pubs.acs.org/10.1021/acsami.4c14420

Notes

The authors declare no competing financial interest.

ACKNOWLEDGMENTS

This work was supported by DOE BES-RENEW award number DE-SC0024611. D.E.A. would like to acknowledge NSF HBCU-UP RIA (HRD 1800795) for partial support in MXene synthesis. The authors also acknowledge the DOD HBCU/MSI instrumentation award (Contract No: W911NF1910522) to acquire HR-TEM (JEOL 2100PLUS) with STEM/EDS capability. XPS and SEM measureemnt were carried out in Joint School of Nanoscience and Nanoengineering, a member of the Southeastern Nanotechnology Infrastructure Corridor and National Nanotechnology Coordinated Infrastructure, which was supported by the National Science Foundation (grant no. ECCS-1542174). The authors thank Dr. Nisha Hiralal Makani, Moses Ashies, and Rabin Dahal for assisting in synthesizing MXene, XPS measurement, and SEM measurement, respectively.

REFERENCES

(1) Gogotsi, Y.; Anasori, B. The Rise of MXenes. *ACS Nano* **2019**, *13* (8), 8491−8494.

(2) Ayodhya, D. A Review of Recent Progress in 2D MXenes: Synthesis, Properties, and Applications. *Diam. Relat. Mater.* **2023**, *132*, 109634.

(3) Naguib, M.; Kurtoglu, M.; Presser, V.; Lu, J.; Niu, J.; Heon, M.; Hultman, L.; Gogotsi, Y.; Barsoum, M. W. Two-Dimensional Nanocrystals Produced by Exfoliation of Ti_3AlC_2. *Adv. Mater.* **2011**, *23* (37), 4248−4253.

(4) Nahirniak, S.; Ray, A.; Saruhan, B. Challenges and Future Prospects of the MXene-Based Materials for Energy Storage Applications. *Batteries* **2023**, *9* (2), 126.

(5) Prenger, K.; Sun, Y.; Ganeshan, K.; Al-Temimy, A.; Liang, K.; Dun, C.; Urban, J. J.; Xiao, J.; Petit, T.; Van Duin, A. C. T.; Jiang, D. E.; Naguib, M. Metal Cation Pre-Intercalated $Ti_3C_2T_x$ MXene as Ultra-High Areal Capacitance Electrodes for Aqueous Supercapacitors. *ACS Appl. Energy Mater.* **2022**, *5* (8), 9373−9382.

(6) Wang, S.; Liu, Y.; Liu, Y.; Hu, W. Effect of HF Etching on Titanium Carbide ($Ti_3C_2T_x$) Microstructure and Its Capacitive Properties. *Chem. Eng. J.* **2023**, *452*, 139512.

(7) Wu, Z.; Shang, T.; Deng, Y.; Tao, Y.; Yang, Q. H. The Assembly of MXenes from 2D to 3D. *Adv. Sci.* **2020**, *7*, 1903077.

(8) Xie, X.; Zhao, M. Q.; Anasori, B.; Maleski, K.; Ren, C. E.; Li, J.; Byles, B. W.; Pomerantseva, E.; Wang, G.; Gogotsi, Y. Porous Heterostructured MXene/Carbon Nanotube Composite Paper with High Volumetric Capacity for Sodium-Based Energy Storage Devices. *Nano Energy* **2016**, *26*, 513−523.

(9) Mateen, A.; Ahmad, Z.; Ali, S.; Hassan, N. U.; Ahmed, F.; Alshgari, R. A.; Mushab, M.; Eldin, S. M.; Ansari, M. Z.; Javed, M. S.; Peng, K. Q. Silicon Intercalation on MXene Nanosheets towards New Insights into a Superior Electrode Material for High-Performance Zn-Ion Supercapacitor. *J. Energy Storage* **2023**, *71*, 108151.

(10) Mashtalir, O.; Naguib, M.; Mochalin, V. N.; Dall'Agnese, Y.; Heon, M.; Barsoum, M. W.; Gogotsi, Y. Intercalation and Delamination of Layered Carbides and Carbonitrides. *Nat. Commun.* **2013**, *4*, 1716.

(11) Chen, H.; Yu, L.; Lin, Z.; Zhu, Q.; Zhang, P.; Qiao, N.; Xu, B. Carbon Nanotubes Enhance Flexible MXene Films for High-Rate Supercapacitors. *J. Mater. Sci.* **2020**, *55*, 1148−1156.

(12) Wu, Y.; Nie, P.; Wu, L.; Dou, H.; Zhang, X. 2D MXene/SnS_2 Composites as High-Performance Anodes for Sodium Ion Batteries. *Chem. Eng. J.* **2018**, *334*, 932−938.

(13) Liang, K.; Matsumoto, R. A.; Zhao, W.; Osti, N. C.; Popov, I.; Thapaliya, B. P.; Fleischmann, S.; Misra, S.; Prenger, K.; Tyagi, M.; Mamontov, E.; Augustyn, V.; Unocic, R. R.; Sokolov, A. P.; Dai, S.; Cummings, P. T.; Naguib, M. Engineering the Interlayer Spacing by Pre-Intercalation for High Performance Supercapacitor MXene Electrodes in Room Temperature Ionic Liquid. *Adv. Funct. Mater.* **2021**, *31*, 2104007.

(14) Liu, S.; Kang, L.; Zhang, J.; Jun, S. C.; Yamauchi, Y. Carbonaceous Anode Materials for Non-Aqueous Sodium- And Potassium-Ion Hybrid Capacitors. *ACS Energy Lett.* **2021**, *6* (11), 4127−4154.

(15) Liu, S.; Kang, L.; Jun, S. C. Challenges and Strategies toward Cathode Materials for Rechargeable Potassium-Ion Batteries. *Adv. Mater.* **2021**, *33* (47), 1−40.

(16) Tsyganov, A.; Vikulova, M.; Artyukhov, D.; Zheleznov, D.; Gorokhovsky, A.; Gorshkov, N. Intercalation Effects on the Dielectric Properties of PVDF/$Ti_3C_2T_x$ MXene Nanocomposites. *Nanomaterials* **2023**, *13* (8), 1337.

(17) Almafie, M. R.; Marlina, L.; Riyanto, R.; Jauhari, J.; Nawawi, Z.; Sriyanti, I. Dielectric Properties and Flexibility of Polyacrylonitrile/Graphene Oxide Composite Nanofibers. *ACS Omega* **2022**, *7* (37), 33087−33096.

(18) Ponnamma, D.; Ninan, N.; Thomas, S. Carbon Nanotube Tube Filled Polymer Nanocomposites and Their Applications in Tissue Engineering. *Appl. Nanomater. Adv. Key Technol.* **2018**, 391−414.

(19) Allen-Perry, K.; Straka, W.; Keith, D.; Han, S.; Reynolds, L.; Gautam, B.; Autrey, D. E. Tuning the Magnetic Properties of Two-Dimensional Mxenes by Chemical Etching. *Materials* **2021**, *14* (3), 694−699.

(20) Gong, H.; Ilavsky, J.; Kuzmenko, I.; Chen, S.; Yan, H.; Cooper, C. B.; Chen, G.; Chen, Y.; Chiong, J. A.; Jiang, Y.; Lai, J. C.; Zheng, Y.; Stone, K. H.; Huelsenbeck, L.; Giri, G.; Tok, J. B. H.; Bao, Z. Formation Mechanism of Flower-like Polyacrylonitrile Particles. *J. Am. Chem. Soc.* **2022**, *144* (38), 17576−17587.

(21) Hashemi, M.; Rahmanifar, M. S.; El-Kady, M. F.; Noori, A.; Mousavi, M. F.; Kaner, R. B. The Use of an Electrocatalytic Redox

Electrolyte for Pushing the Energy Density Boundary of a Flexible Polyaniline Electrode to a New Limit. *Nano Energy* **2018**, *44*, 489−498.
(22) Zhou, Y.; Jin, P.; Zhou, Y.; Zhu, Y. High-Performance Symmetric Supercapacitors Based on Carbon Nanotube/Graphite Nanofiber Nanocomposites. *Sci. Rep.* **2018**, *8* (1), 9005−9008.
(23) Alonzo, S. M. M.; Bentley, J.; Desai, S.; Bastakoti, B. P. Hydrothermal Synthesis of Hierarchical Microstructure Tungsten Oxide/Carbon Nanocomposite for Supercapacitor Application. *Sci. Rep.* **2023**, *13* (1), 21732.
(24) Lukatskaya, M. R.; Mashtalir, O.; Ren, C. E.; Dall'Agnese, Y.; Rozier, P.; Taberna, P. L.; Naguib, M.; Simon, P.; Barsoum, M. W.; Gogotsi, Y. Cation Intercalation and High Volumetric Capacitance of Two-Dimensional Titanium Carbide. *Science* **2013**, *341* (6153), 1502−1505.
(25) Maleski, K.; Mochalin, V. N.; Gogotsi, Y. Dispersions of Two-Dimensional Titanium Carbide MXene in Organic Solvents. *Chem. Mater.* **2017**, *29* (4), 1632−1640.
(26) Luo, Y.; Que, W.; Tang, Y.; Kang, Y.; Bin, X.; Wu, Z.; Yuliarto, B.; Gao, B.; Henzie, J.; Yamauchi, Y. Regulating Functional Groups Enhances the Performance of Flexible Microporous MXene/Bacterial Cellulose Electrodes in Supercapacitors. *ACS Nano* **2024**, *18*, 11675−11687.
(27) Eom, Y.; Kim, B. C. Solubility Parameter-Based Analysis of Polyacrylonitrile Solutions in N,N-Dimethyl Formamide and Dimethyl Sulfoxide. *Polymer* **2014**, *55* (10), 2570−2577.
(28) Zhang, J.; Usman, K. A. S.; Judicpa, M. A. N.; Hegh, D.; Lynch, P. A.; Razal, J. M. Applications of X-Ray-Based Characterization in MXene Research. *Small Methods* **2023**, *7* (8), 1−16.
(29) Shekhirev, M.; Shuck, C. E.; Sarycheva, A.; Gogotsi, Y. Characterization of MXenes at Every Step, from Their Precursors to Single Flakes and Assembled Films. *Prog. Mater. Sci.* **2021**, *120*, 100757.
(30) Dixit, P.; Maiti, T. A Facile Pot Synthesis of (Ti_3AlC_2) MAX Phase and Its Derived MXene ($Ti_3C_2T_x$). *Ceram. Int.* **2022**, *48* (24), 36156−36165.
(31) Yoon, Y.; Le, T. A.; Tiwari, A. P.; Kim, I.; Barsoum, M. W.; Lee, H. Low Temperature Solution Synthesis of Reduced Two Dimensional Ti3C2MXenes with Paramagnetic Behaviour. *Nanoscale* **2018**, *10* (47), 22429−22438.
(32) Sarycheva, A.; Gogotsi, Y. Raman Spectroscopy Analysis of the Structure and Surface Chemistry of Ti_3C_2Tx MXene. *Chem. Mater.* **2020**, *32* (8), 3480−3488.
(33) Natu, V.; Benchakar, M.; Canaff, C.; Habrioux, A.; Célérier, S.; Barsoum, M. W. A Critical Analysis of the X-Ray Photoelectron Spectra of $Ti_3C_2T_z$ MXenes. *Matter* **2021**, *4* (4), 1224−1251.
(34) Liu, S.; Kang, L.; Zhang, J.; Jung, E.; Lee, S.; Jun, S. C. Structural Engineering and Surface Modification of MOF-Derived Cobalt-Based Hybrid Nanosheets for Flexible Solid-State Supercapacitors. *Energy Storage Mater.* **2020**, *32*, 167−177.
(35) Kang, K. N.; Lee, H.; Kim, J.; Kwak, M. J.; Jeong, H. Y.; Kim, G.; Jang, J. H. Co3O4 Exsolved Defective Layered Perovskite Oxide for Energy Storage Systems. *ACS Energy Lett.* **2020**, *5* (12), 3828−3836.
(36) Kang, L.; Liu, S.; Zhang, Q.; Zou, J.; Ai, J.; Qiao, D.; Zhong, W.; Liu, Y.; Jun, S. C.; Yamauchi, Y.; Zhang, J. Hierarchical Spatial Confinement Unlocking the Storage Limit of MoS2 for Flexible High-Energy Supercapacitors. *ACS Nano* **2024**, *18* (3), 2149−2161.
(37) Adomavičiūtė-Grabusovė, S.; Ramanavičius, S.; Popov, A.; Šablinskas, V.; Gogotsi, O.; Ramanavičius, A. Selective Enhancement of Sers Spectral Bands of Salicylic Acid Adsorbate on 2d $Ti_3C_2T_x$-Based Mxene Film. *Chemosensors* **2021**, *9* (8), 223.
(38) Yang, Q.; Eder, S. J.; Martini, A.; Grützmacher, P. G. Effect of Surface Termination on the Balance between Friction and Failure of $Ti_3C_2T_x$ MXenes. *npj Mater. Degrad.* **2023**, *7* (1), 6−8.
(39) Bao, Z.; Lu, C.; Cao, X.; Zhang, P.; Yang, L.; Zhang, H.; Sha, D.; He, W.; Zhang, W.; Pan, L.; Sun, Z. Role of MXene Surface Terminations in Electrochemical Energy Storage: A Review. *Chin. Chem. Lett.* **2021**, *32* (9), 2648−2658.
(40) Ashie, M. D.; Bastakoti, B. P. Photocatalytic Hydrogen Evolution Using Mesoporous Honeycomb Iron Titanate. *Small* **2024**, *20*, 2310927.
(41) Wang, Y.; Fugetsu, B.; Wang, Z.; Gong, W.; Sakata, I.; Morimoto, S.; Hashimoto, Y.; Endo, M.; Dresselhaus, M.; Terrones, M. Nitrogen-Doped Porous Carbon Monoliths from Polyacrylonitrile (PAN) and Carbon Nanotubes as Electrodes for Supercapacitors. *Sci. Rep.* **2017**, *7*, 40259−40311.
(42) Wahid, M.; Parte, G.; Phase, D.; Ogale, S. Y. Yogurt: a novel precursor for heavily nitrogen doped supercapacitor carbon. *J. Mater. Chem. A* **2015**, *3* (3), 1208−1215.
(43) Ghidiu, M.; Lukatskaya, M. R.; Zhao, M. Q.; Gogotsi, Y.; Barsoum, M. W. Conductive Two-Dimensional Titanium Carbide "clay" with High Volumetric Capacitance. *Nature* **2014**, *516* (7529), 78−81.
(44) Dall, Y.; Rozier, P.; Taberna, P.; Gogotsi, Y.; Dall, Y.; Rozier, P.; Taberna, P.; Gogotsi, Y.; Simon, P. Capacitance of Two-Dimensional Titanium Carbide (MXene) and MXene/Carbon Nanotube Composites in Organic Electrolytes. *J. Power Sources* **2016**, *306*, 510−515.
(45) Yun, C.; Hwang, S. Analysis of the Charging Current in Cyclic Voltammetry and Supercapacitor's Galvanostatic Charging Profile Based on a Constant-Phase Element. *ACS Omega* **2021**, *6* (1), 367−373.
(46) Bastakoti, B. P.; Oveisi, H.; Hu, C. C.; Wu, K. C. W.; Suzuki, N.; Takai, K.; Kamachi, Y.; Imura, M.; Yamauchi, Y. Mesoporous Carbon Incorporated with In_2O_3 Nanoparticles as High-Performance Supercapacitors. *Eur. J. Inorg. Chem.* **2013**, *2013* (7), 1109−1112.
(47) Rastabi, S. A.; Sarraf-Mamoory, R.; Razaz, G.; Blomquist, N.; Hummelgård, M.; Olin, H. Treatment of $NiMoO_4$/Nanographite Nanocomposite Electrodes Using Flexible Graphite Substrate for Aqueous Hybrid Supercapacitors. *PLoS One* **2021**, *16*, 1−11.
(48) Bastakoti, B. P.; Huang, H. S.; Chen, L. C.; Wu, K. C. W.; Yamauchi, Y. Block Copolymer Assisted Synthesis of Porous α-Ni(OH)2 Microflowers with High Surface Areas as Electrochemical Pseudocapacitor Materials. *Chem. Commun.* **2012**, *48* (73), 9150−9152.
(49) Quan, L.; Zhang, H.; Xu, L. The Non-Isothermal Cyclization Kinetics of Amino-Functionalized Carbon Nanotubes/Polyacrylonitrile Composites by in Situ Polymerization. *J. Therm. Anal. Calorim.* **2015**, *119* (2), 1081−1089.
(50) Ardizzone, S.; Fregonara, G.; Trasatti, S. Inner and "Outer" Active Surface of RuO_2 Electrodes. *Electrochim. Acta* **1990**, *35*, 263−267.
(51) Nashim, A.; Pany, S.; Parida, K. M. Systematic Investigation on the Charge Storage Behavior of $GdCrO_3$ in Aqueous Electrolyte. *J. Energy Storage* **2021**, *42*, 103145.
(52) Pholauyphon, W.; Charoen-amornkitt, P.; Suzuki, T.; Tsushima, S. Perspectives on Accurately Analyzing Cyclic Voltammograms for Surface- and Diffusion-Controlled Contributions. *Electrochem. commun.* **2024**, *159*, 107654.
(53) Deebansok, S.; Deng, J.; Le Calvez, E.; Zhu, Y.; Crosnier, O.; Brousse, T.; Fontaine, O. Capacitive Tendency Concept alongside Supervised Machine-Learning toward Classifying Electrochemical Behavior of Battery and Pseudocapacitor Materials. *Nat. Commun.* **2024**, *15* (1), 1133.
(54) Lazanas, A. C.; Prodromidis, M. I. Electrochemical Impedance Spectroscopy−A Tutorial. *ACS Meas. Sci. Au* **2023**, *3* (3), 162−193.
(55) Mei, B. A.; Munteshari, O.; Lau, J.; Dunn, B.; Pilon, L. Physical Interpretations of Nyquist Plots for EDLC Electrodes and Devices. *J. Phys. Chem. C* **2018**, *122* (1), 194−206.
(56) Mainka, J.; Gao, W.; He, N.; Dillet, J.; Lottin, O. A General Equivalent Electrical Circuit Model for the Characterization of MXene/Graphene Oxide Hybrid-Fiber Supercapacitors by Electrochemical Impedance Spectroscopy−Impact of Fiber Length. *Electrochim. Acta* **2022**, *404*, 139740.
(57) Grahame, D. C. Fiftieth Anniversary: Mathematical Theory of the Faradaic Admittance. *J. Electrochem. Soc.* **1952**, *99*, 370−385.

https://doi.org/10.1021/acsami.4c14420
ACS Appl. Mater. Interfaces 2024, 16, 64784−64796

(58) Yu, H. C.; Adler, S. B.; Barnett, S. A.; Thornton, K. Simulation of the Diffusional Impedance and Application to the Characterization of Electrodes with Complex Microstructures. *Electrochim. Acta* **2020**, *354*, 136534.
(59) KC, B. R.; Kumar, D.; Bastakoti, B. P. Block Copolymer-Mediated Synthesis of TiO_2/RuO_2 Nanocomposite for Efficient Oxygen Evolution Reaction. *J. Mater. Sci.* **2024**, *59* (23), 10193−10206.
(60) Dahal, R.; Ray, S. K.; Pathiraja, G.; Bastakoti, B. P. Low-Temperature Fabrication of Morphology-Controllable Cu_2O for Electrochemical CO_2 Reduction. *J. Mater. Sci.* **2024**, *59* (30), 13896−13907.
(61) De, S.; Maity, C. K.; Sahoo, S.; Nayak, G. C. Polyindole Booster for $Ti_3C_2T_x$ MXene Based Symmetric and Asymmetric Supercapacitor Devices. *ACS Appl. Energy Mater.* **2021**, *4* (4), 3712−3723.
(62) Chavan, R. A.; Kamble, G. P.; Dhavale, S. B.; Rasal, A. S.; Kolekar, S. S.; Chang, J. Y.; Ghule, A. V. NiO@MXene Nanocomposite as an Anode with Enhanced Energy Density for Asymmetric Supercapacitors. *Energy Fuels* **2023**, *37* (6), 4658−4670.

https://doi.org/10.1021/acsami.4c14420
ACS Appl. Mater. Interfaces 2024, 16, 64784−64796